Lawrence Berkeley National Laboratory
LBL Publications

Title

An Induction Linac Approach to Phase Rotation of a Muon Bunch in the Production Region of a m+ m- Collider

Permalink

https://escholarship.org/uc/item/7ff0796j

Author

Turner, W C

Publication Date

1995-11-01

LBL-38009
UC-414
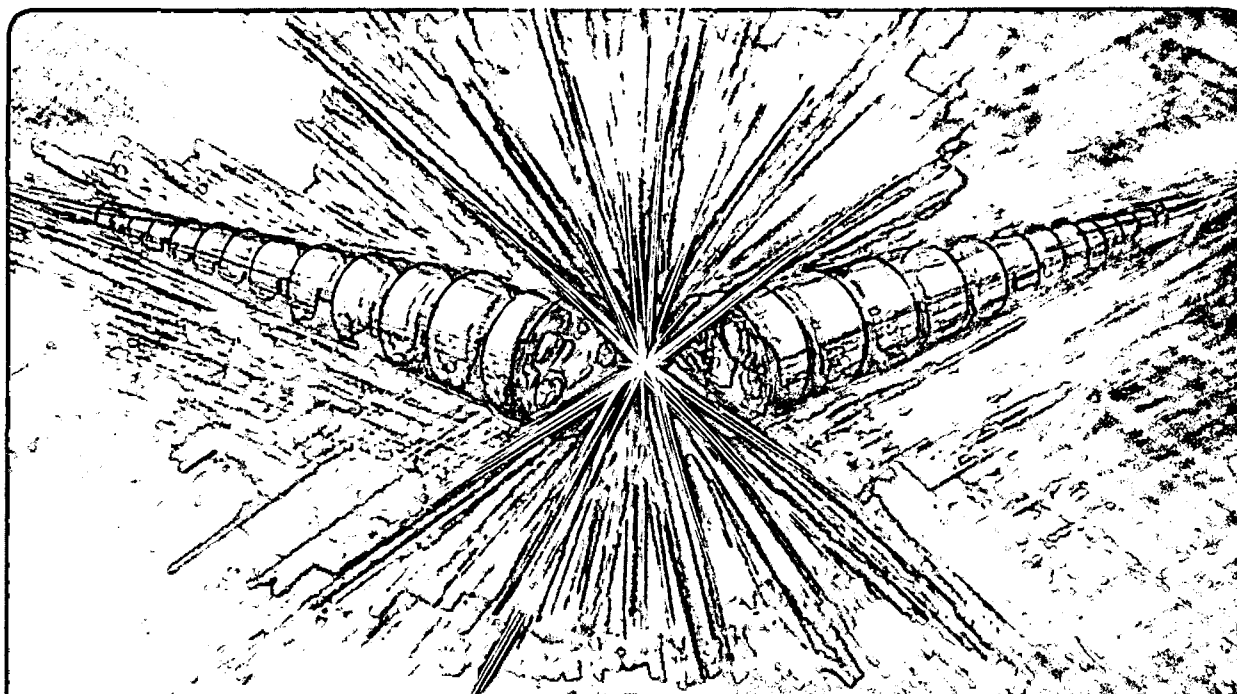
Lawrence Berkeley Laboratory
UNIVERSITY OF CALIFORNIA

Accelerator & Fusion Research Division

Presented at the Ninth Advanced ICFA Beam Dynamics Workshop:
Beam Dynamics and Technology Issues for μ+–μ- Colliders,
Montauk, NY, October 15–20, 1995, and to be published in
the Proceedings

An Induction Linac Approach to Phase Rotation of a Muon Bunch in the Production Region of a μ+–μ- Collider

W.C. Turner

November 1995

DISCLAIMER

An Induction Linac Approach to Phase Rotation of a Muon Bunch in the Production Region of a μ^+-μ^- Collider*

William C. Turner

Lawrence Berkeley National Laboratory
University of California
Berkeley, CA 94720

November 22, 1995

An Induction Linac Approach to Phase Rotation of a Muon Bunch in the Production Region of a μ^+–μ^- Collider

William C. Turner

Lawrence Berkeley National Laboratory
1 Cyclotron Rd.
Berkeley, CA 94720

Abstract. The possibility of using an induction linac for phase rotation, or equivalently flattening the head to tail mean energy sweep, of a muon bunch in the production region of a μ^+–μ^- collider is examined. Axial spreading of an accelerating bunch is analyzed and the form of appropriate induction cell voltage waveforms is derived. A set of parametric equations for the induction accelerator structure is given and specific solutions are presented which demonstrate the technological feasibility of the induction linac approach to phase rotation.

INTRODUCTION

In this paper we consider the possibility of using an induction linac for longitudinal phase rotation of the muon bunch in the production region of a μ^+–μ^- collider(1). The induction linac is to be inserted in a region following the decay of pions into muons and prior to entering the muon phase space cooling region. The instantaneous muon energy spread is reduced from $\Delta E/E \sim \pm 100\%$ to $\sim \pm 10\%$ by allowing the bunch to drift and spread longitudinally. The instantaneous mean energy of muons arriving at a given axial location is highest at the head of a bunch and the lowest at the tail. An induction linac is then used to flatten the head to tail sweep of mean energy from $\sim 300\%$ to a few per cent by applying an appropriately shaped voltage waveform to the acceleration gaps. In order to analyze the feasibility of this idea it is necessary to characterize the muon pulse as a function of time. Figs. 1 and 2 show the results of typical Monte Carlo muon production calculations presented in this way(2). For these calculations the proton energy is 10 GeV, rms pulse width is 3 nsec and 0.2 muons per proton are captured in the decay channel at $z = 201$ m from the target. In Fig. 1 the mean instantaneous muon energy is plotted as a function of time of arrival at $z = 201$ m. (Throughout this paper "muon energy" is always total energy, including the rest mass.) At the head of the pulse the mean energy is 1.2 GeV, decreasing to 0.5 GeV at $T = 38.3$ nsec. With the exception of the Monte Carlo data point at the head of the pulse, the mean energy is reasonably well fit with an exponential function;

$$\langle E(GeV) \rangle = 0.21 + 0.79 e^{-T(n\,sec)/38.3}. \qquad (1)$$

Because the muons are relativistic ($\beta = 0.9945$ at 1 GeV) axial drift is only partially successful in reducing the instantaneous energy spread to the desired goal of ± 10%. In particular at the head of the pulse the muon spectrum extends above 2 GeV, compared to the mean 1.2 GeV. In practice it won't be possible to use muons above some cutoff energy and introducing such a cutoff will bring the Monte Carlo data at the head of the bunch into closer agreement with eqn. 1. For the feasibility discussion below we will assume eqn. 1 is a reasonable approximation of the mean muon energy.
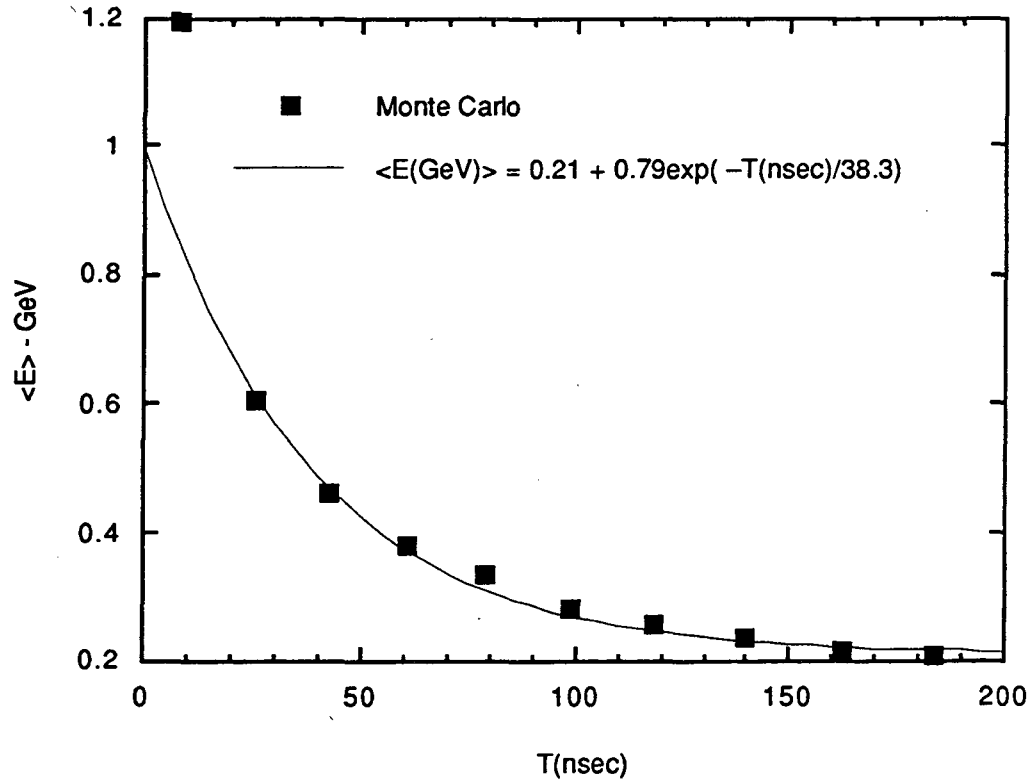
FIGURE 1. Mean muon energy versus time at z = 201 m from the proton target.

The instantaneous muon current is plotted versus arrival time in Fig. 2, again at z = 201 m from the production target. The Monte Carlo results have been normalized to 5×10^{13} protons on the target producing 2×10^{13} captured muons. At the head of the bunch the current is 76 A, decreasing to 21 A at $T = 50$ nsec. Except for the first two Monte Carlo data points, these data are also reasonably well fit by an exponential function;

$$I(A) = 57e^{-T(n\sec)/50}.$$

(2)

2

Again cutting off high energy muons at the head of the bunch will tend to bring the Monte Carlo results into closer agreement with eqn. 2 and we will assume eqn. 2 is a reasonable approximation of the muon current. The integrated number of muons represented by eqn. 2 is 1.8×10^{13}.

At this point it is worth making a few observations based on Figs. 1 and 2. First, in order to flatten the mean energy to E_S a summation of voltage waveforms equal to the difference between E_S and eqn. 1 would be applied;

$$\sum_i eV_i(GeV) = E_S(GeV) - 0.21 - 0.79e^{-T(nsec)/38.3}. \qquad (3)$$

Depending on the choice of E_S, the head may be decelerated and the tail accelerated ($E_S > 1$ GeV), the head not accelerated ($E_S = 1$ GeV) or the entire
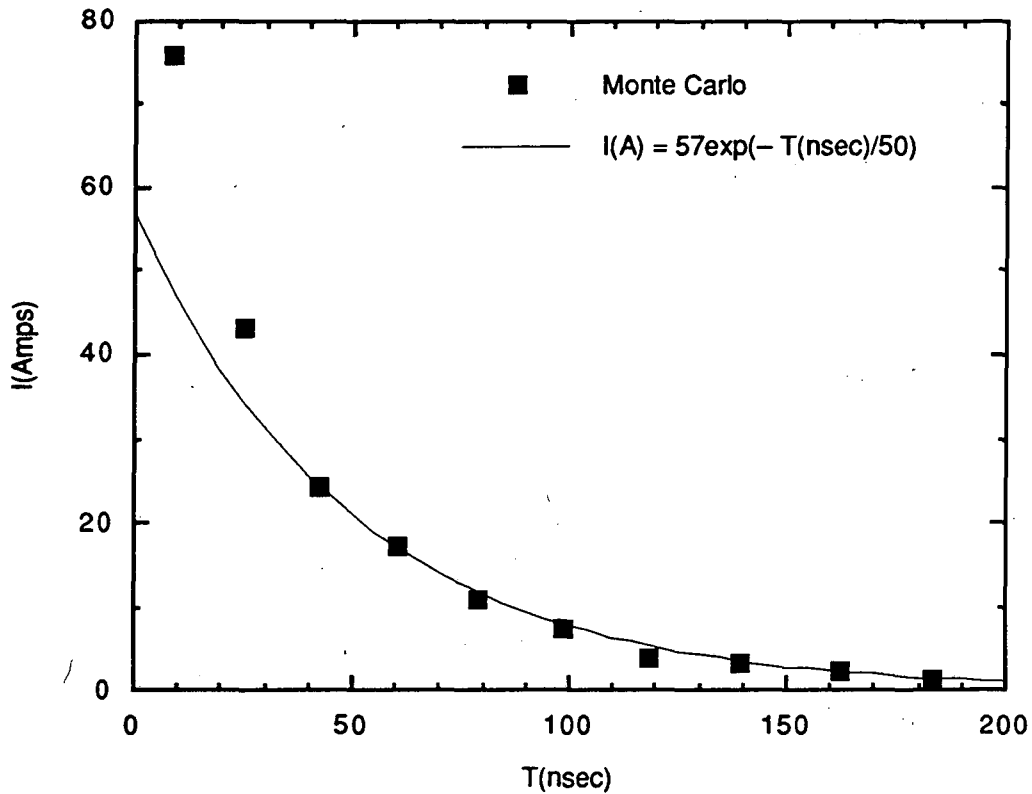
FIGURE 2. Muon current at z = 201 m.

pulse accelerated ($E_S > 1$ GeV). The first choice leads to bipolar waveforms which, while possible, presents a complication in the design of the pulsed power system feeding the induction cells. The third choice doesn't seem interesting in the absence of a rationale for accelerating muons to greater than 1 GeV before injection into the cooling section. Therefore we consider the second, $E_S = 1$ GeV.

For a reasonable accelerating gradient $V' \sim 1$ MV/m, the total length of induction accelerator would be $\sim 0.5 - 1$ km. The issue of magnitude of accelerating gradient and a consistent induction cell structure will be discussed in detail below. The summation of waveforms indicated by eqn. 3 will need to be applied to a large number of induction cells extending over hundreds of meters. The bunch will continue to spread as it propagates through the accelerator and, as a consequence, the detailed shape of the accelerating waveforms will change and the time scale will lengthen from beginning to end of the accelerator compared to what is indicated in eqn. 3. This will be discussed quantitatively in the following section. Nevertheless it is clear from Fig. 1 that the risetime of the voltage waveforms will be of the order of $40 - 50$ nsec. This is slow enough to allow flexibility in the radial size and the capacitance of the induction cells. As we will see this is fortunate. The very large radius of the beam tube $R_w = 15$ cm and the 7 T superconducting focusing solenoids that are required by the large transverse momentum spread of the muons dictates that the induction cores be placed at a large radius $\sim 2 - 3$ R_w.

Referring to Fig. 2, the muon current is less than 100 A, rather low compared to the kiloampere beams usually encountered in electron induction accelerators. This together with the large beam tube radius implies that the beam breakup instability will have a growth length many times the length of the accelerator so this instability does not introduce significant design concerns. The muon beam current is also low compared to what we can expect for an induction core leakage current of $\sim$ few kA. Pulse distortion by beam current loading will therefore be negligible and this is a design advantage. We need only be concerned with the effective load resistance of the induction core, the cell capacitance and the pulse power impedance to determine the shape of the voltage waveform. The accelerator efficiency will be low $\sim 0.1\%$ but that is a minor concern for this application. Finally we note from Fig. 2 that the Monte Carlo data extend to 183 nsec, however only 18% of the muons arrive after 80 nsec. Since the power consumed by the induction accelerator increases linearly with pulse width and is nearly independent of the beam loading it becomes relatively inefficient and expensive to accelerate the last few trailing muons. Here we will somewhat arbitrarily cut off the accelerated muons at 80 nsec. The number of muons from zero to 80 nsec represented by eqn. 2 is 1.4×10^{13} muons per 5×10^{13} protons.

In Fig. 3 we have indicated in a schematic way the layout of induction cells and focusing solenoids for an assumed module length $L_m = 1$ m. The 7 T superconducting solenoids and cryostats are shown extending from an inside radius $R_w = 15$ cm to an outside radius 30 cm and extending over an axial length fraction 60%. The induction cells are represented by induction cores, vacuum insulators and vacuum acceleration gaps. The induction cores have been stacked radially outside the insulators rather than axially in series. This maximizes the axial length fraction for magnetic material and therefore maximizes the effective accelerating gradient. The acceleration gaps are assumed to extend over the 40% of axial length between solenoids and to extend inward to $R_w = 15$ cm. For the magnetic induction cores two conceptual possibilities are indicated. In the first case, Fig. 3(a), the cores are located entirely between the solenoids. This minimizes the interference between induction cells and solenoids and places the induction cores at the minimum possible radius. It is essential that negligible magnetic flux from the solenoids leak out of the beam channel and reach the induction cores so the induction cores are shown outside the solenoid structure in Fig. 3(a). In addition it will be necessary to divide the solenoid and induction cell structure more finely than indicated

4

schematically in Fig. 3(a) to avoid flux leakage into the cores. In the second case, Fig. 3(b), the induction cores are allowed to extend over the outside of the
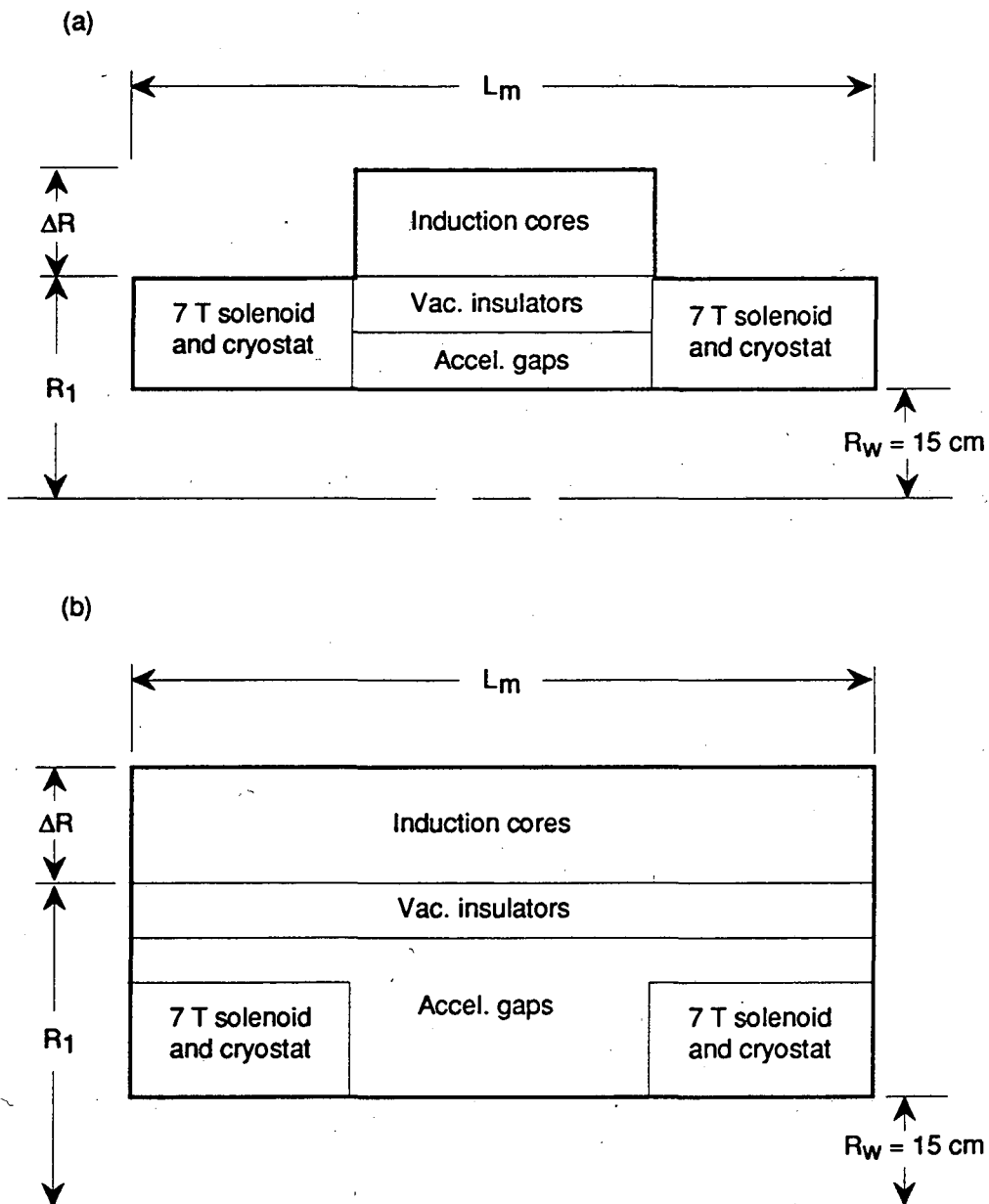
(a)

(b)

FIGURE 3. Schematics of induction cell components;(a) minimum interference between solenoids and induction cells and (b) maximum axial length for induction cores.

solenoids. Since more axial length is available for magnetic material, the accelerating gradient is increased up to a factor 2.5. However, now the vacuum insulators must be placed entirely outside the 7 T solenoid structure and the vacuum acceleration gaps must be mapped from outside the solenoids to the gaps between solenoids. All of this increases the radius, volume and weight of the cores as well as the cell capacitance. To see what is possible some detailed calculations have been done. The results are in the last section of the paper.

The remainder of the paper is divided into three sections. The first section describes the longitudinal dynamics of the muon bunch as it drifts and is accelerated. The second section presents an induction cell model and uses the model to analyze the induction core geometry and achievable accelerating gradient. The final section presents a table of parameters for four accelerator cases.

LONGITUDINAL DYNAMICS OF A MUON PULSE

We now derive the relationship between muon energy and time of arrival at a given axial position in the accelerator with the parametric dependence on accelerating gradient given explicitly. The time of arrival (T) is measured relative to an unaccelerated reference particle within the bunch labeled by the subscript "s". It turns out to be simplest to find $T(E,z)$ and then invert the result numerically to get $E(T,z)$. As a byproduct we also get the time dependence of the self consistent accelerator gap waveforms $V(T,z)$. As the muons propagate the change in their arrival time relative to the reference particle is given by;

$$\frac{\partial T}{\partial z} = \frac{1}{c}\left(\frac{1}{\beta_z} - \frac{1}{\beta_{s,z}}\right) \, . \tag{4}$$

where $c\beta_z$ is the velocity component parallel to the accelerator axis and $\beta_z^2 + \beta_\perp^2 = 1 - 1/\gamma^2$. In order to integrate eqn. 4 we imagine the bunch is subdivided into infinitesimal slices and apply an accelerating gradient $\gamma' = V'/mc^2$ to each slice. Space charge forces are unimportant since $\beta \sim 1, \gamma \gg 1$. The transverse velocity component is treated by writing $\beta_\perp^2$ in terms of transverse momentum and then taking the rms value within a slice: $\langle \beta_\perp^2 \rangle = \langle p_\perp^2 \rangle / (m\gamma c)^2 = \alpha/\gamma^2$. For numerical calculations we set the rms transverse momentum equal to the square of the cutoff momentum of a particle with an orbit passing through the axis of the solenoid focusing channel with $B = 7$ T and $R_w = 15$ cm; $\langle p_\perp^2 \rangle = (158 MeV/c)^2$, $\alpha = 2.25$. γ' must vary from slice to slice in order to flatten the energy distribution but for each slice is conveniently chosen to be independent of z. This is a simple way of insuring that all slices reach the reference energy at the same axial location. We label each slice with a subscript "i" which can be thought of as its mean energy at $z = 0$. We also have in mind only cases where the mean energy is a monotonically decreasing function of arrival time and specifically exclude the possibility of one slice overtaking another. Owing to

the spread of energies within a slice, the individual muons rearrange themselves somewhat amongst the slices, but we don't need to keep track of that. Then,

$$\gamma_i(z) = \gamma_i(z=0) + \gamma'_i z$$
$$= \frac{E_i(z)}{mc^2} \qquad (5)$$

and

$$T_i(z) = \frac{1}{c\gamma'_i}\left\{\sqrt{(\beta\gamma)_i^2 - \alpha} - \sqrt{(\beta\gamma)_{i,z=0}^2 - \alpha}\right\} - \frac{z}{c\beta_{s,z}} + T_i(z=0). \qquad (6)$$

If $\gamma'_i = 0$, eqn. 6 reduces to

$$T_i(z) = \frac{1}{c}\left(\frac{\gamma_i}{\sqrt{\gamma_i^2 - \left(1+\alpha^2\right)}} - \frac{\gamma_s}{\sqrt{\gamma_s^2 - \left(1+\alpha^2\right)}}\right)z + T_i(z=0).$$

$$(7)$$

Now we choose the magnitude of γ'_i to achieve the desired result of flattening the mean energy sweep;

$$\gamma'_i = \frac{V'_i}{mc^2}$$
$$= \frac{V'_m}{mc^2}\frac{E_s - E_i(z=0)}{\Delta E}. \qquad (8)$$

where ΔE is the magnitude of energy sweep that is to be reduced to zero and V'_m is the maximum accelerating gradient. The accelerator length is $z_m = \Delta E / V'_m$. We note that eqn. 5 maps the energy at $z = 0$ to the energy at z, eqn. 6 maps the energy at z to the arrival time at z and eqn. 8 maps the energy at $z = 0$ to the accelerating gradient. These may be used to obtain the mean muon energy and the accelerating gradient as functions of the arrival time within a bunch and the propagation distance z as shown in Figs. 4 and 5. For the initial condition we take eqn. 1 for $E_i(z=0)$ versus T. In Fig. 4a there is no acceleration so the muon bunch is simply continuing to spread out, noticeably more in the low energy tail than at the head of the bunch. At $z = 0$ km in Fig. 4a, the 0.3 GeV muons at the tail arrive 82.5 nsec after the 1 GeV muons at the head of the bunch; by the time the bunch reaches $z = 1$ km this time delay has grown to 1,000 nsec. In Fig. 4b we have added acceleration, chosen $E_s = 1$ GeV so the muons at the head of the bunch are not accelerated, $\Delta E = 0.7$ GeV and applied a maximum accelerating gradient $V_m' = 1$ MV/m to the tail of the pulse with energy 0.3 GeV at $z = 0$. The muon bunch reaches a flat energy distribution at $z_m = 700$ m. Acceleration quickly slows the
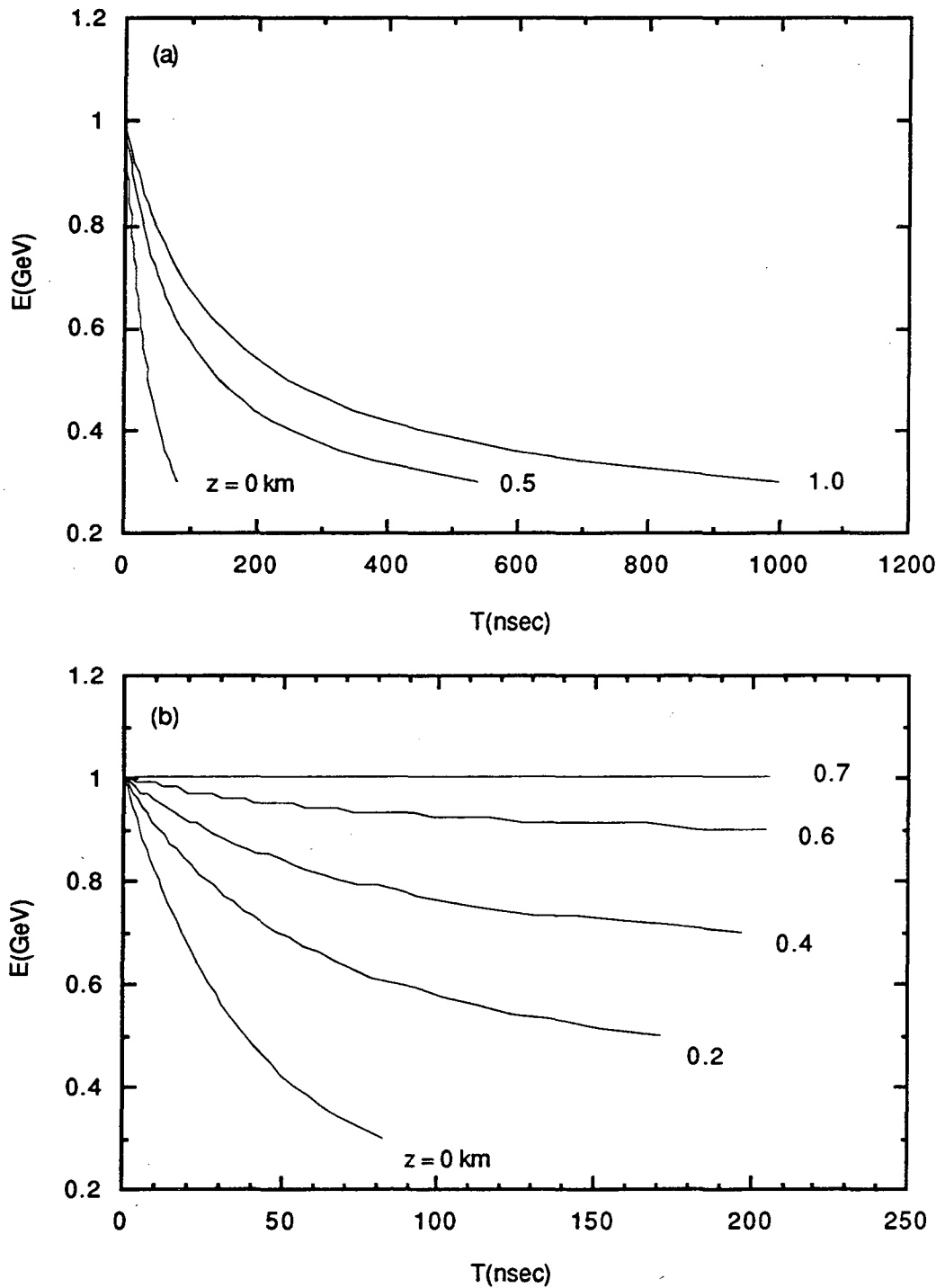
FIGURE 4. Muon pulse spreading and energy flattening with (a) drift only and (b) acceleration. For (b) the maximum acceleration gradient equals 1.0 MeV/m at the tail of the pulse. z = 0 is 201 m from the proton target.

spreading of the bunch so the width only reaches 205 nsec by the end of the induction linac. The decrease in spreading is most noticeable after the first 200 m so one should eventually consider the possibility of increasing the accelerating gradient at the front of the accelerator. The condition of constant γ' can be met piecewise.

The accelerating gradient versus time that is consistent with Fig. 4b is shown for three axial locations $z = 0$, 0.2 and 0.7 km in Fig. 5. The time duration of the applied voltage gradient increases with distance because of the increase in differential arrival time of each muon slice relative to the head of the bunch (eqn. 4) and our stated condition of applying a constant accelerating gradient to each slice. One can check that the arrival times for the tail of the bunch relative to the head are consistent in Fig. 4b and Fig. 5. This is true for intermediate slices as well; muons with $E = 0.5$ GeV at $z = 0$ km arrive at $T = 38.2$ nsec, 0.2 km at $T = 66.8$ nsec and 0.7 km at $T = 85.2$ nsec and experience constant gradient $V' = 0.71$ MV/m etc.. The integrated volt-seconds/m for the three waveforms shown in Fig. 5 are .055, .122 and .134 volt-seconds/m at $z = 0$, 0.2 and 0.7 km respectively. In
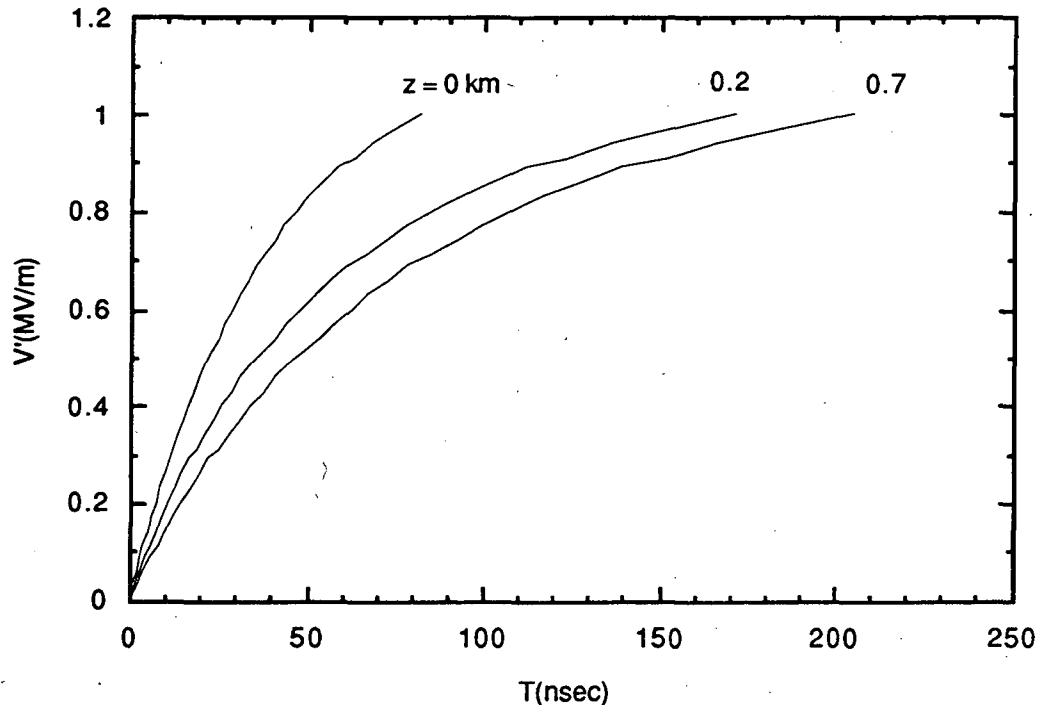
FIGURE 5. Acceleration waveforms at three axial locations from beginning to end of the induction linac.

addition to the lengthening time scale of the voltage pulse with distance there is also a change of the waveshape because low energy muons spread more rapidly than high energy ones. However the distortion is not too great and the simple exponential at $z = 0$ with $\tau_v = 38.3$ nsec maps reasonably accurately (i.e. within a couple of per cent) for our purposes to exponential waveforms at $z = 0.2$ and

0.7 km with $\tau_v = 66.8$ and 85.2 nsec. Eqn. 6 may be used to calculate the mapping of τ_v .

MODEL EQUATIONS

A schematic of an induction cell is shown in Fig. 6 which also defines some of the geometric quantities that will appear in the mathematical description. There are four components to the cell: (1) the high voltage pulsed power feed, (2) the magnetic core, (3) the vacuum insulator and (4) the acceleration gap. The induction core has axial length w and radial width ΔR. The inside and outside radii of the magnetic core are R_1 and R_2. The high voltage pulsed power lead enters along one side of the core, encircles it and returns to ground. The magnetic core volume behind the vacuum insulator is filled with insulating dielectric fluid. There are three insulating gap widths indicated: the dielectric gap g_d, the vacuum insulator gap g_s and the acceleration gap g_v. These must withstand dielectric breakdown, vacuum surface flashover and vacuum breakdown respectively. The angle between the insulator surface and the metal electrode surfaces on the vacuum side is shown to be $\sim 25^o$ to 45° to maximize the breakdown limiting field strength. The re-entrant acceleration gap prevents radiation from the beam channel reaching the insulator surface and possibly initiating breakdown. The primary concern here is shielding the synchrotron radiation coming from electrons and positrons from muon decay. The total length of the induction cell is L_c.

We now turn to the equations for determining the magnitudes of the geometric quantities in terms of materials properties and parameters of the accelerator. There are three primary equations for the induction core; (1) the cell axial length, (2) the volt-seconds of the magnetic core and (3) the voltage risetime. A fourth equation describes the axial length needed for voltage insulation and shielding the vacuum insulator. The cell axial length is the minimum required by either the magnetic core region or the vacuum insulator plus accelerator gap region. The requirements of voltage insulation and shielding the vacuum insulator will determine a maximum accelerating gradient. For gradients chosen to be at or below this maximum the cell dimensions are then determined by the magnetic core region and there is a leftover marginal length for voltage insulation and shielding. We begin by treating the magnetic core region and then turn to voltage insulation and shielding of the vacuum insulator.

A simple exponential waveform applied to the induction cells is adequate for flattening the energy sweep;

$$V(T) = V_0 \left(1 - e^{-\frac{T}{\tau_v}} \right) . \tag{9}$$

Then the length of the cell L_c is related to the voltage and gradient applied at the end of the pulse by;

$$L_c = (1 + f_s)w + g_d$$

$$= f_c \frac{V_0}{V_m'} \left(1 - e^{-\frac{T_{max}}{\tau_v}} \right) \quad , \tag{10}$$
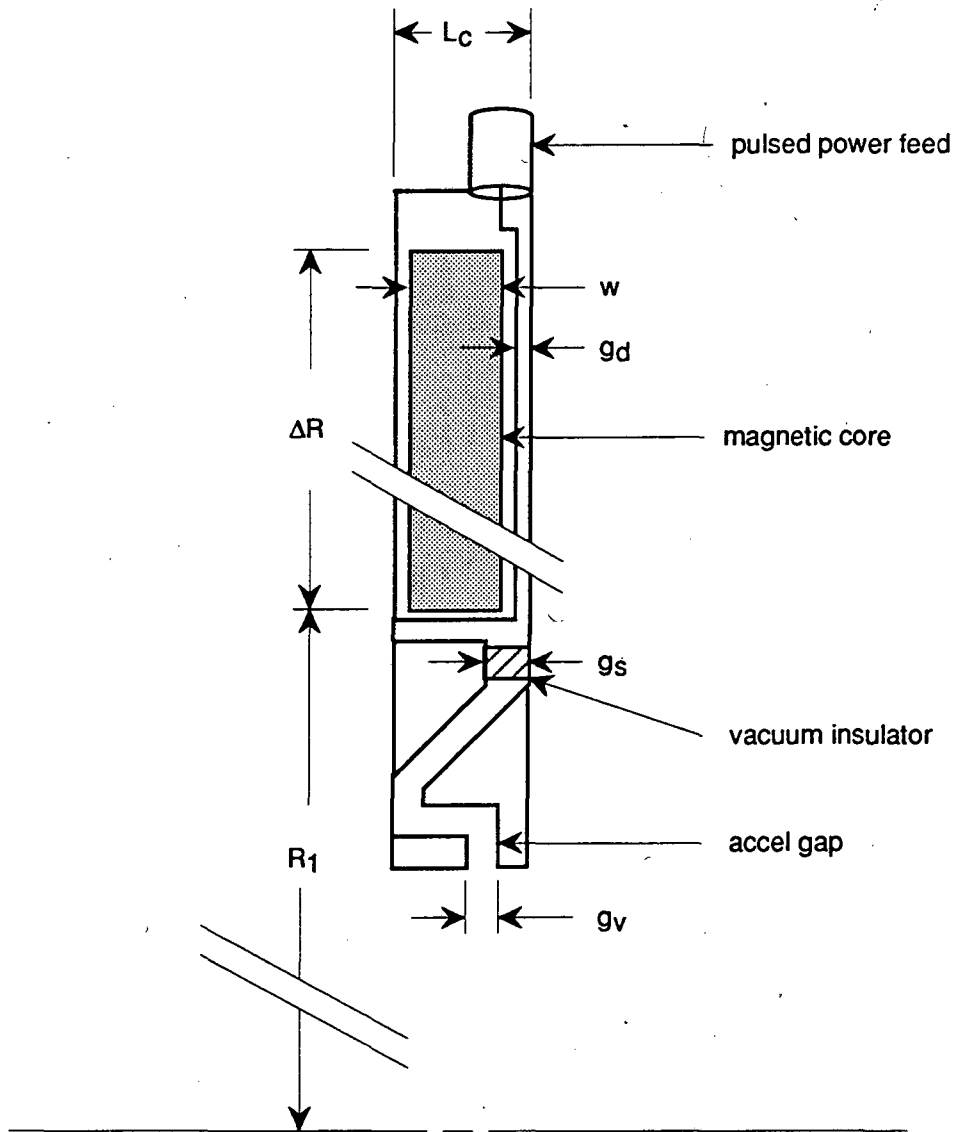

FIGURE 6. A schematic illustration of an induction cell showing the definition of some of the geometric quantities used in the model calculations.

where f_S is the fraction of cell length relative to the width of the induction core that must be allowed for mechanical structure, and f_C is the fraction of accelerator length occupied by induction cells. The accelerating gradient has been defined so it is the effective gradient over the entire length of accelerator and not over the reduced length occupied by induction cells.

The volt-seconds applied to the induction core is the integral of eqn. 9 and setting this equal to the magnetic flux swing of the induction core we obtain;

$$\frac{p_f \Delta B w \Delta R}{V_0 \tau_v} = \left(\frac{T_{max}}{\tau_v} - 1\right) - e^{-\frac{T_{max}}{\tau_v}} \tag{11}$$

where ΔB is the change in magnetic induction and p_f is the effective packing fraction of magnetic core material.

Hysteresis losses of the magnetic core material (eddy currents and domain wall dissipation) dominate the impedance of the induction core viewed by the pulsed power circuitry. These losses may be represented by an effective load resistance R_L which will be discussed in a moment. The pulsed power impedance is then chosen to match R_L to minimize reflected energy and the voltage risetime may be written as;

$$\tau_v = \frac{R_L C}{2} + \tau_s \tag{12}$$

where C is the cell capacitance and τ_s is the intrinsic risetime of the pulsed power circuitry.

We now turn to expressions for C and R_L so that eqn. 12 can be written in terms of the cell geometry. The internal cell capacitance is dominated by the capacitance of the dielectric gap g_d. There are additional smaller contributions from the vacuum insulator and acceleration gap which we neglect. In addition it will be useful to add some external capacitance C_{ext} which is not shown in Fig. 6. The external capacitance has two functions: (1) it serves as a tuning element for adjusting τ_v and (2) it results in an increased dielectric gap g_d which, although not necessary for voltage holding in most cases we have examined, is useful for achieving gap dimensions that seem reasonable for mechanical fabrication tolerances. We then obtain;

$$C = \varepsilon \pi (R_1 + R_2) \frac{\Delta R}{g_d} + C_{ext} \tag{13}$$

where ε is the dielectric constant of the insulating fluid. In numerical calculations we will choose $C_{ext} = 0.5*C$.

The voltage applied to the induction cell is related to the core averaged time rate of change of magnetic induction $\dot{B}$ by;

$$V = p_f \dot{B} w \Delta R. \tag{14}$$

If the instantaneous core loss power per unit volume averaged over the core volume is denoted by $\dot{e}_L$ then the product of cell voltage and load current I_L is;

$$VI_L = p_f \pi (R_1 + R_2) w \Delta R * \dot{e}_L. \tag{15}$$

Taking the ratio of eqns. 15 and 14 we obtain the load current,

$$I_L = \pi (R_1 + R_2) \frac{\dot{e}_L}{\dot{B}} \tag{16}$$

and the ratio of eqns. 14 and 16 defines the load impedance,

$$R_L = \frac{p_f w \Delta R}{\pi (R_1 + R_2)} \frac{\dot{B}^2}{\dot{e}_L} . \tag{17}$$

To complete the equations for numerical analysis an expression is needed for the specific core loss $\dot{e}_L$. The particular material we have in mind is an amorphous ferromagnetic alloy, Metglas 2605SC, chosen for its very high change in magnetic induction from negative remanance to saturation $\Delta B > 2.5$ T(3). The core loss data that are available measure the dynamic hysteresis energy loss per unit volume per cycle for square wave excitation to saturation as a function of $\dot{B} = \Delta B / T_{sat}$(4). For $\dot{B}$ exceeding 1 T/μsec the data are reasonably well approximated by a linear dependence of e_L on $\dot{B}$. At lower values of $\dot{B}$ the increase in hysteresis loss is not as steep but this is well below our range of interest. To further parameterize e_L we also factor out the magnitude of the flux swing since if the core is not driven to saturation we expect the loss to drop proportionally for a given $\dot{B}$. This is valid for material with reasonably square shaped hysteresis loops. For Metglas 2605SC we then obtain;

$$e_L = \alpha_L \Delta B \dot{B} \tag{18}$$

and,

$$\dot{e}_L = \alpha_L \dot{B}^2 \tag{19}$$

with $\alpha_L = 7.9 \times 10^{-5}$ J$\cdot$sec/T^{2}m^3 and $\dot{B} > 1$ T/μsec. In our applications the excitation is not square wave but we will assume the validity of eqn. 19 for the instantaneous specific core loss appearing in eqns. 16 and 17. We then obtain for the load current and load resistance;

$$I_L = \pi(R_1 + R_2)\alpha_L \dot{B} \tag{20}$$

and,

$$R_L = \frac{p_f w \Delta R}{\pi(R_1 + R_2)} \frac{1}{\alpha_L}. \tag{21}$$

We notice that with the parameterizations of eqns. 18 and 19 the load current and applied voltage have the same time dependence and R_L is time independent.

Choosing $C_{ext} = 0.5*C$ and inserting eqns. 13 and 21 into eqn. 12, the dielectric gap width is related to core dimensions and risetime by;

$$g_d = \frac{p_f \varepsilon}{\alpha_L} \frac{w(\Delta R)^2}{\tau_v - \tau_s}. \tag{22}$$

Eqns. 10, 11 and 22 can now be combined to solve for the dielectric gap width g_d and the core dimensions w and ΔR. First we eliminate g_d and ΔR to obtain a quadratic equation for w;

$$w^2 - \frac{f_c}{1 + f_s} \frac{V_0}{V'_m} \left(1 - e^{-\frac{T_{max}}{\tau_v}} \right) w + \frac{A_1 A_2^2}{1 + f_s} = 0, \tag{23}$$

where

$$A_1 = \frac{p_f \varepsilon}{\alpha_L} \frac{1}{\tau_v - \tau_s}, \tag{24}$$

and

$$A_2 = \frac{V_0 \tau_v}{p_f \Delta B} \left[\left(\frac{T_{max}}{\tau_v} - 1 \right) - e^{-\frac{T_{max}}{\tau_v}} \right]. \tag{25}$$

The solutions for w, ΔR and g_d are then;

$$w_\pm = \frac{1}{2} \frac{f_c}{1 + f_s} \frac{V_0}{V'_m} \left(1 - e^{-\frac{T_{max}}{\tau_v}} \right) \pm \frac{1}{2} \sqrt{\left(\frac{f_c}{1 + f_s} \frac{V_0}{V'_m} \left(1 - e^{-\frac{T_{max}}{\tau_v}} \right) \right)^2 - 4 \frac{A_1 A_2^2}{1 + f_s}}, \tag{26}$$

$$\Delta R_\pm = \frac{A_2}{w_\pm} \tag{27}$$

and

$$g_\pm = A_1 w_\pm (\Delta R_\pm)^2. \tag{28}$$

From the form of eqn. 26 it is clear that the following inequality must be satisfied in order for solutions to exist;

$$\frac{f_c}{1+f_s} \frac{V_0}{V'_m} \left(1 - e^{-\frac{T_{max}}{\tau_v}} \right) > 2 \left(\frac{A_1 A_2^2}{1+f_s} \right)^{1/2} \tag{29}$$

and this implies an upper bound on the accelerating gradient,

$$V'_m < \frac{1}{2} \frac{f_c}{(1+f_s)^{1/2}} \frac{p_f \Delta B}{\tau_v} \left(\frac{\alpha}{p_f \varepsilon} (\tau_v - \tau_s) \right)^{1/2} \frac{1 - e^{-\frac{T_{max}}{\tau_v}}}{\left(\frac{T_{max}}{\tau_v} - 1 \right) - e^{-\frac{T_{max}}{\tau_v}}}. \tag{30}$$

Physically, as the accelerating gradient increases the cell length must decrease in order to fit more cells into a given space. This is done by decreasing w and increasing ΔR so the volt-seconds product per core stays the same. Meanwhile the dielectric gap g_d increases to keep the capacitance and risetime from increasing. However the overall cell length decreases because the increase in g_d is more than offset by the decrease in w. Eventually g_d becomes equal in magnitude to $(1+f_s)*w$ (see eqn. 10) and the increase in g_d can no longer be compensated by a decrease in w. At this point a limiting maximum accelerating gradient has been reached.

In Figs. 7, 8 and 9 we have plotted the induction cell geometric parameters $w_\pm$, $\Delta R_\pm$ and $g_{d\pm}$ versus accelerating gradient V'_m. Results are shown for induction cells occupying fractions $f_c = 0.4$ and 0.8 of the accelerator length. Assumed values for the parameters appearing in eqns. 23 to 28 are given Table 1. The cell voltage $V_0 = 50$ kV was chosen with consideration of how the pulse power system might be configured. In principle one could choose spark gaps, thyratrons or saturating magnetic cores for the final stage switch into the induction cores since they can all be configured to handle the required power level. Spark gaps could allow operation up to $V_0 = 250$ kV. However electrode erosion would require replacement after a few million pulses, or a day of operation at 30 Hz, so they are ruled out. Saturating magnetic cores have been shown to switch coaxial lines charged up to ~ 200 kV at kHz rep rates and high power thyratrons are commercially available for switching up to ~ 50 kV so either of these seems possible. Fifty kilovolts was chosen as a compromise between these two possibilities; a saturating magnetic core discharging a coaxial line charged to $2V_0 = 100$ kV or a thyratron discharging a Blumlein line charged to $V_0 = 50$ kV.

The voltage risetime τ_v and duration T_{max} appear in the equations for $w_{\pm}$, $\Delta R_{\pm}$ and $g_{d\pm}$ and as we have seen in Fig. 5, these vary along the length of the accelerator. To be specific we have presented the results for the beginning of the accelerator $z = 0$ ($\tau_v = 38.3$ nsec, $T_{max} = 82.5$ nsec) in Figs. 7a, 8a and 9a and at the end $z = z_m$ in Figs. 7b, 8b and 9b. Since the length of the accelerator depends

TABLE 1. Parameter values used for the evaluation of Figs. 7 to 10.

Parameter	Symbol	Value
Cell voltage, kV	V_0	50
Pulse power intrinsic risetime, nsec	τ_s	10
Induction core packing fraction	p_f	.75
Insulating fluid relative dielectric constant	$\varepsilon/\varepsilon_0$	3.4
Structure fraction	f_s	0.2
Magnetic induction flux swing, T	ΔB	2.5
Induction core loss parameter, J·sec/T^{2}m^3	α_L	7.9×10^5

on the accelerating gradient τ_v and T_{max} do also; for each value of V'_m, τ_v and T_{max} are calculated using eqn. 6.

In Figs. 7 to 9 the positive roots of eqn. 27 to 28 are plotted as the solid lines and the negative roots as dashed lines. The negative roots lead to core widths w that are less than the insulating gap width g_v and are impractically thin for fabrication, so only the positive roots are useful. Looking at the positive root solutions, the range of accelerating gradients that seem possible (1 to 2.5 MV/m for $w > 1$ cm, $g_v > 1$ mm) are several times larger than what one ordinarily encounters for electron induction accelerators. The reasons for this are: (1) choosing a core aspect ratio $\Delta R/w > 1$, (2) stacking the insulator and induction cores radially rather than axially and (3) using induction cores fabricated from Metglas with $\Delta B = 2.5$ T rather than Ni-Zn ferrite with $\Delta B = 0.6$ T. The comparatively slow risetime $\tau_v > 38$ nsec is the factor which allows this.

So far we have dealt with the induction core geometry and voltage waveshape requirements. We now turn to the requirements of high voltage insulation. Because of the light beam loading we do not have to worry about significant mismatch overvoltage if the beam is absent. The length of a cell cannot be less than what is required to prevent high voltage breakdown and therefore high voltage insulation imposes an upper bound on accelerating gradient V'_m that is independent of the
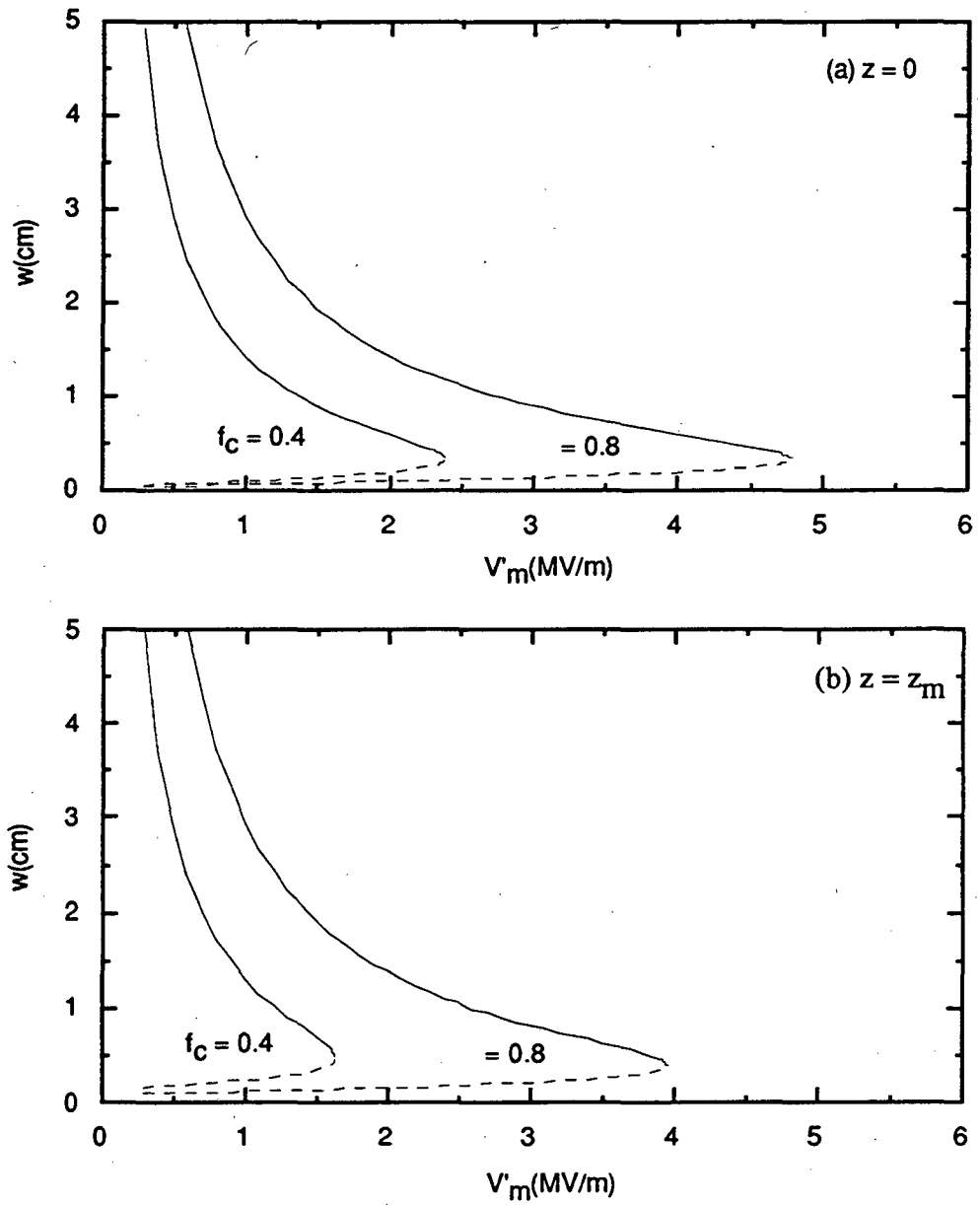
FIGURE 7. Axial width of the induction cell magnetic core versus accelerating gradient (a) at the beginning of the induction linac and (b) at the end. Induction cell voltage is $V_0 = 50$ kV. Results are shown for magnetic cores occupying fractions $f_c = 0.4$ and 0.8 of the length of the accelerator.
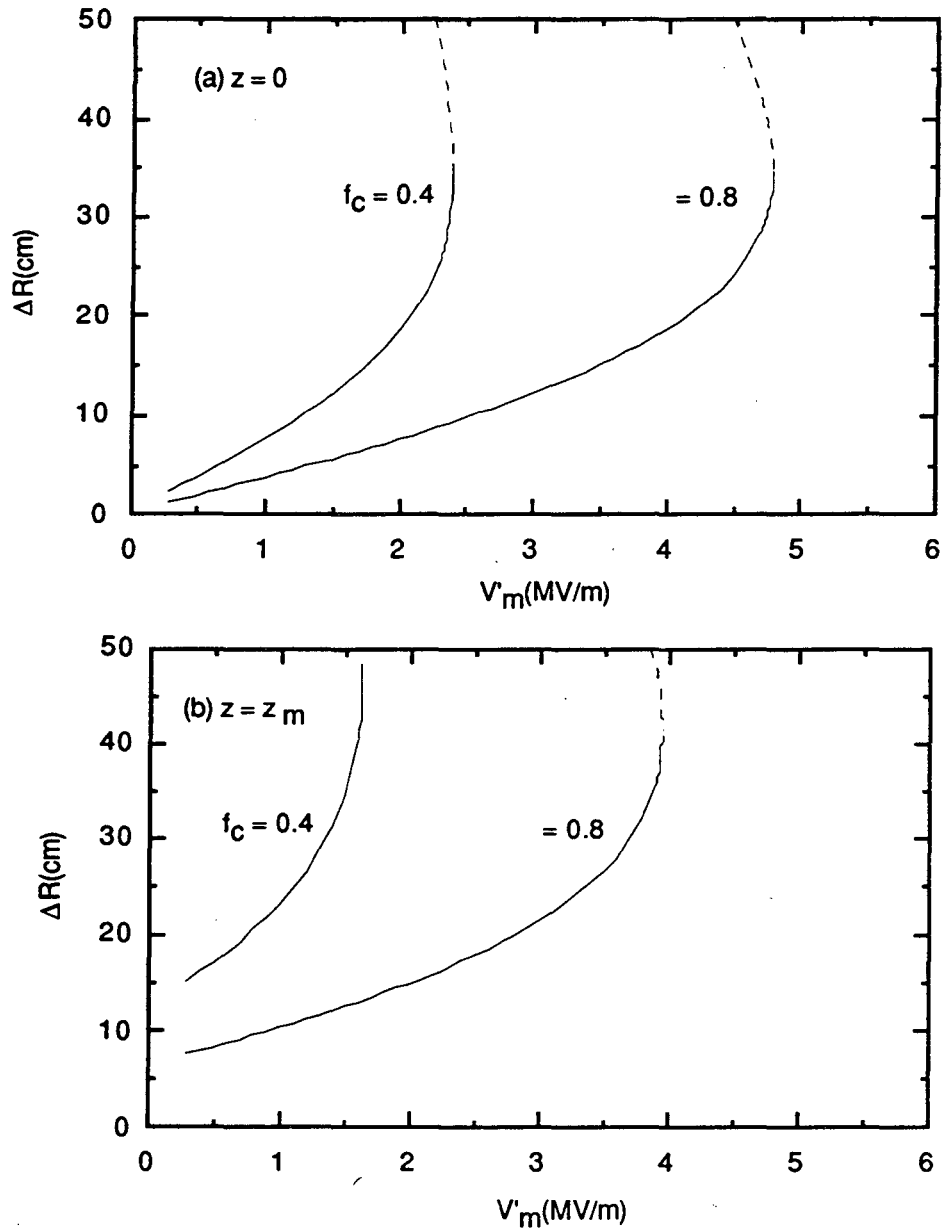
FIGURE 8. Radial width of the induction cell magnetic core versus accelerating gradient (a) at the beginning of the induction linac and (b) at the end. Conditions are the same as Fig. 7.
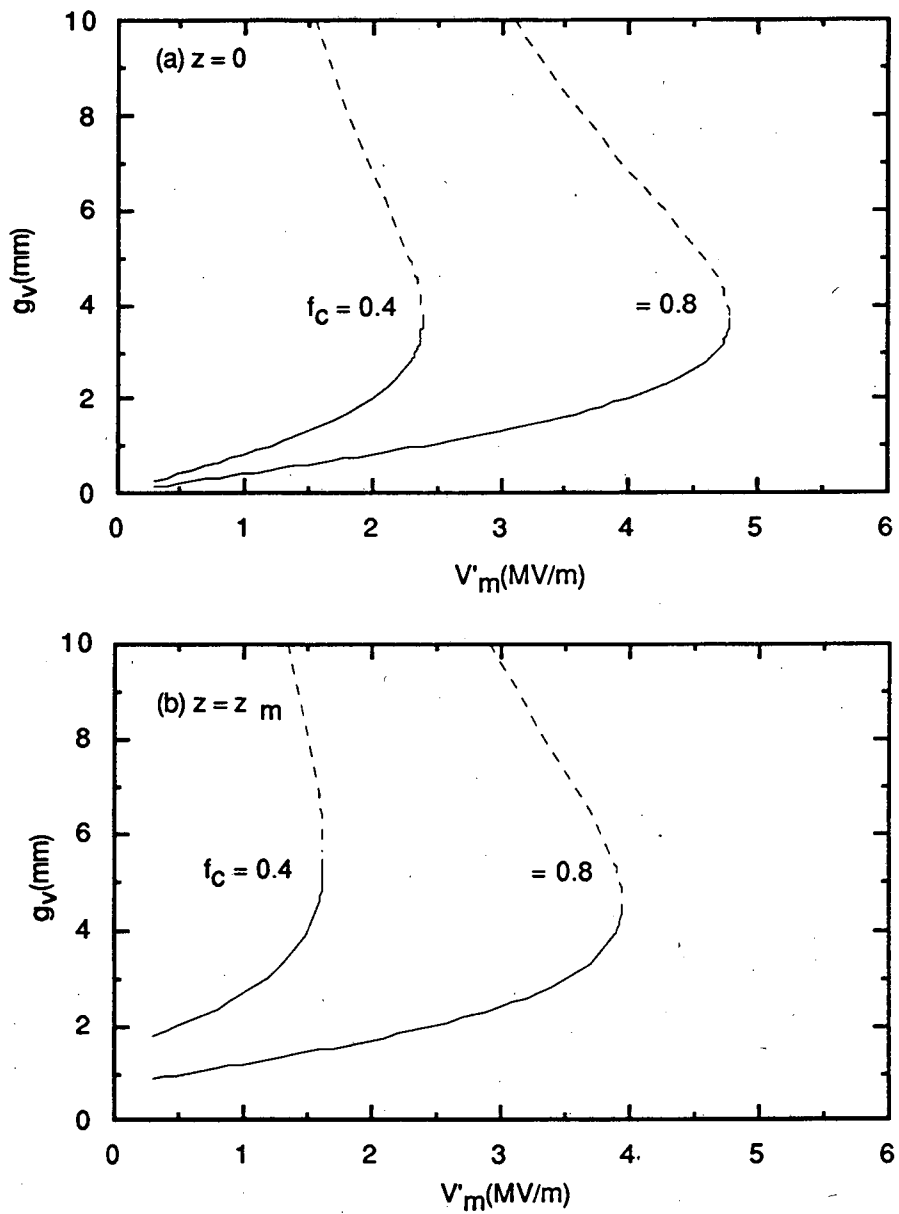
FIGURE 9. Dielectric insulation gap width versus accelerating gradient (a) at the beginning of the accelerator and (b) at the end. Conditions are the same as Fig. 7.

considerations of induction core size that have been discussed above. We first discuss the size of each insulation gap and then turn to the voltage breakdown limited accelerating gradient.

For the dielectric fluid we choose transformer oil and require

$$g_d > \frac{V_0}{E_{oil}} \qquad (31)$$

with the breakdown electric field strength in oil taken to be (5);

$$E_{oil}(MV/cm) \approx \frac{0.5}{\tau_p^{1/3}(\mu \sec)A^{1/10}(cm^2)}. \qquad (32)$$

The pulse width τ_p is the time the voltage waveform exceeds 63% of its maximum value (i.e. $T > \tau_v$ in eqn. 9) and A is the electrode area. The dependencies on τ_p and A are rather weak so we don't need precise values. Taking $\tau_p = .12\ \mu sec$ and $A \sim 3,000\ cm^2$, $E_{oil} = 0.45$ MV/cm and for $V_0 = 50$ kV, we obtain $g_d > 1.1$ mm. The plots in Fig. 9 satisfy this constraint except at the lowest accelerating gradients. If more margin is needed it can easily be obtained by simply increasing g_d and at the same time increasing the external trim capacitance fraction C_{ext}/C so the risetime is unchanged. Another possibility would be to insert several layers of .025 mm Kapton in the dielectric gap.

The vacuum insulator is assumed to be Lexan (polycarbonate, $\varepsilon/\varepsilon_0 = 3.0$) or Rexolite (cross linked polystyrene, $\varepsilon/\varepsilon_0 = 2.5$). Care needs to be taken to avoid field enhancement at the triple points where vacuum, metal and insulator meet. Usually this is done by recessing the insulator slightly in the electrode surface. Scaling relations for surface flashover electric field strength as a function of pulse duration, gap width and surface area are not generally available. However for the size of insulators we are dealing with and for pulse duration ~ 110 nsec above $0.63\ V_0$ we take a limiting surface flashover field strength $E_s = 50$ kV/cm. The insulator height g_s should then satisfy

$$g_s > \frac{V_0}{E_s}, \qquad (33)$$

or for $V_0 = 50$ kV, $g_s > 1$ cm. Similarly for vacuum breakdown initiated on the metal electrode surfaces we take a limiting field strength $E_v = 100$ kV/cm and obtain for the acceleration gap,

$$g_v > \frac{V_0}{E_v}, \qquad (34)$$

or for $V_0 = 50$ kV, $g_v > 0.5$ cm. Care would need to be taken in the details of the shape of the electrodes between the vacuum insulator and acceleration gap,

particularly at bends, to avoid excessive local enhancement of the field strength compared to eqn. 34.

We now turn to the voltage insulation limited accelerating gradient. In order to shield the insulator from the muon beam channel the sum of the vacuum insulator height and vacuum acceleration gap must be less than the cell length, or equivalently the following inequality must be obeyed,

$$
\begin{aligned}
\Delta_s &= L_c - g_v - g_s - f_s w \\
&= w + g_d - g_s - g_v \quad . \\
&> 0
\end{aligned}
\tag{35}
$$

In eqn. 35 we have subtracted the allowance for structural width $f_s w$ supporting the induction core since this would presumably be extended to the insulation region. Δ_s has been plotted versus accelerating gradient in Fig. 10, again at the beginning (Fig. 10a) and end (Fig. 10b) of the accelerator. For these calculations the previously calculated w_+ and g_{d+} in Figs. 7 and 9 have been used. For the conditions we have assumed ($V_0 = 50$ kV, $g_s = 1.0$ cm and $g_v = 0.5$ cm) the voltage insulation limited accelerating gradient defined by $\Delta_s = 0$ is ~ 1 MV/m for f_c = 0.4 and ~ 2 MV/m for f_c = 0.8 and not significantly different at $z = 0$ and $z = z_m$.

SPECIFICATION OF ACCELERATOR PARAMETERS

In this final section we give some examples of accelerator parameters. Four cases are considered: (1) V'_m = 1 MV/m, f_c = 0.4, ΔB = 2.5 T, (2) V'_m = 2 MV/m, f_c = 0.8, ΔB = 2.5 T, (3) V'_m = 1 MV/m, f_c = 0.8, ΔB = 2.5 T and (4) V'_m = 1 MV/m, f_c = 0.8, ΔB = 1.25 T. The corresponding accelerator parameters are given in Table 2. The voltage gradients have been chosen to be consistent with the induction cell and voltage insulation requirements. An induction cell voltage V_0 = 50 kV has been assumed for all cases. The fractional width of an induction cell relative to the width of the induction core that is allowed for mechanical structure (f_s in eqn. 10) has been set equal to 0.2. The cell capacitances given in Table 2 are half due to internal structure and half external. The induction core magnetic material is assumed to be Metglas 2605SC with packing fraction p_f = 0.75.

Where it makes a difference, the parameters tabulated in Table 2 are for the last cell which has the largest volt-second requirement (Fig. 5). For the V'_m = 1 MV/m cases the axially averaged volt-seconds per cell is reduced by 14% and for V'_m = 2 MV/m by 10.1%. If this reduction in volt-seconds were accomplished simply by reducing the radial width of the induction cores, keeping the axial length and voltage V_0 the same for all cells, then the total power and weight for the four cases in Table 2 are reduced by 18%, 11.6%, 15.6% and 17.2%. The numbers given for these totals in the last two lines of Table 2 reflect this reduction so the total power is not equal to the number of cells times the power per cell shown in Table 2 etc..

The first case in Table 2 was chosen as an example of minimum interference between focusing solenoids and induction cells with the cells only occupying a fraction f_c = 0.4 of the entire accelerator length (Fig. 3a). This case also puts the
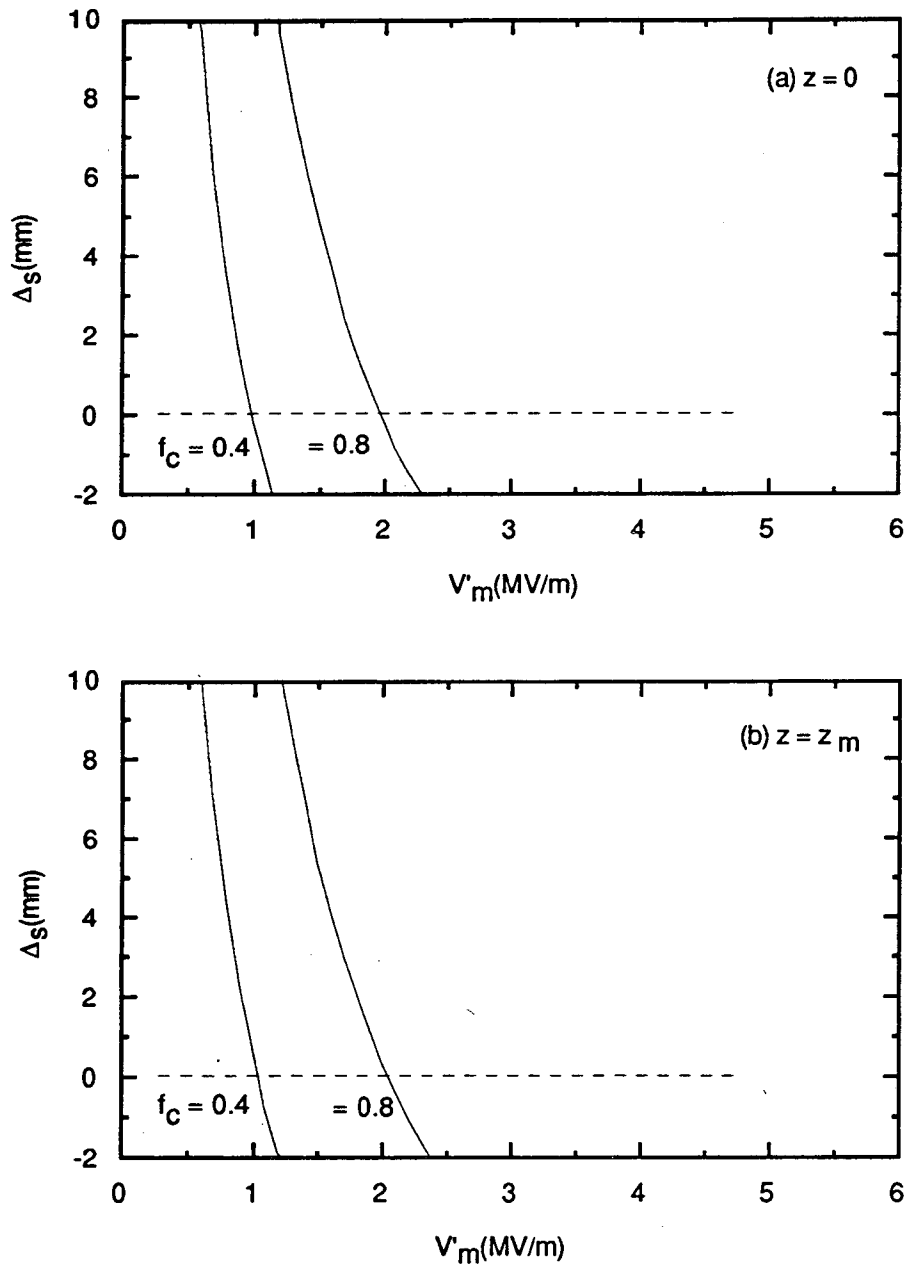
FIGURE 10. Margin for shielding the vacuum insulator from the muon beam channel; (a) at the beginning of the accelerator and (b) at the end. Conditions are the same as Fig. 7.

induction cores at the smallest possible radius $R_1 \sim 30$ cm and therefore minimizes their weight, 43 kg per cell) for given volt-seconds. The axial length of induction core for a single cell is 1.3 cm and the radial width 23 cm. The axial length is a

TABLE 2. Induction linac parameters for four choices of accelerating gradient V'_m and axial length core fraction f_c: (1) $f_c = 0.4$, $V'_m = 1$ MV/m, $\Delta B = 2.5$ T, (2) $f_c = 0.8$, $V'_m = 2$ MV/m, $\Delta B = 2.5$ T, (3) $f_c = 0.8$, $V'_m = 1$ MV/m, $\Delta B = 2.5$ T and (4) $f_c = 0.8$, $V'_m = 1$ MV/m, $\Delta B = 1.25$ T.

Parameter	(1)	(2)	(3)	(4)
Voltage gradient, MV/m	1.0	2.0	1.0	1.0
Cell voltage, kV	50	50	50	50
Axial length fraction for cores, f_c	0.4	0.8	0.8	0.8
Cell length, cm	1.82	1.81	3.64	3.64
Accelerator length, m	700	350	700	700
Number of cells	15,383	15,506	15,383	15,383
Rep. rate, Hz	30	30	30	30
Pulse length, nsec[a]	205.34	143.89	205.34	205.34
Cell voltage risetime, nsec[a]	85.2	61.71	85.2	85.2
Volt seconds per cell[a]	6.39e-3	4.41e-3	6.39e-4	6.39e-3
Core flux swing, T	2.5	2.5	2.5	1.25
dB/dt, T/μsec[a]	12.2	17.4	12.2	6.09
Core loss per cycle, kJ/m^3 [a]	2.4	3.4	2.4	0.6
Inside magnetic core radius, cm	30	42	39	39
Core axial length, cm	1.30	1.37	2.94	2.60
Core radial width, cm[a]	23.1	14.9	10.2	23.1
Dielectric gap width, mm	2.63	1.67	1.16	5.26
Cell capacitance, nF[a]	13.8	16.7	14.7	8.40
Core leakage resistance, Ohms[a]	10.9	6.21	10.3	17.9
Core leakage current, peak, kA[a]	2.51	4.26	2.67	1.53
Core weight per cell, kg[a]	43.0	34.6	45.6	105
Hysteresis energy loss per cell per pulse, J[a]	0.424	0.487	0.450	0.258
Capacitance charging energy per cell per pulse, J[a]	0.429	0.509	0.455	0.261
Mismatch energy per cell per pulse, J[a]	0.560	0.741	0.595	0.341
Total magnetic core weight, tonne[b]	542	474	592	1,337
Total avg. power, MW[b]	17.8	23.9	19.5	10.9

[a] The numbers given for these quantities are for the last cell. Axially averaged values are less by 10 to 20%.

[b] Computed for axially averaged cell parameters.

factor of two or so less than one usually encounters with tape wound Metglas cores but seems doable. The length of the accelerator is 0.7 km, the total number of induction cells is ~ 15,400, the total weight of Metglas 2605SC is 542 tonne and the average pulsed power delivered to the induction cells is 17.8 MW. The energy delivered to a cell is approximately evenly divided between hysteresis loss (14.1 J), charging the cell capacitance (14.3 J) and mismatch power reflected from the cell (18.7 J). Unless the hysteresis loss is removed the induction core would reach the Curie temperature in a few hours so it is necessary to provide some cooling. A flow rate of the dielectric insulating fluid ~ 25 gm/sec would be sufficient to hold the maximum temperature rise inside the core to ~ 10°K. The core leakage current during a pulse ("peak current") is 2.5 kA, which is approximately three orders of magnitude greater than the muon current. The time average incremental power delivered to the muon beam is 25.9 kW, so dividing by the average pulsed power, the overall efficiency is 0.15 per cent.

For the second case the voltage gradient is doubled by increasing the fraction of accelerator length occupied by induction cells to $f_c = 0.8$ (Fig. 3b). This shortens the length of the accelerator to 0.35 km and reduces the pulse width from 205 nsec to 144 nsec. The reduced pulse width results in a decrease in volt-seconds required for the induction cores and a decrease in their weight. The decrease in weight is partially offset by the larger inside diameter since now the vacuum insulators must fit over the outside of the solenoid structure. Furthermore, the shorter pulse results in a higher hysteresis loss per unit volume and the average power increases 34% to 23.9 MW.

The third case is similar to the second with $f_c = 0.8$ but the accelerating gradient has been reduced to $V'_m = 1.0$ MV/m so the length is again 0.7 km. The main change here is that the axial length of the induction core is increased to 2.9 cm which is in the range of what is usually encountered for tape wound Metglas cores. Because the cores have larger radius their weight and hysteresis loss are slightly greater than the first case with the same gradient.

For the fourth case in Table 2, the total magnetic induction flux swing of the induction core material has been reduced by one half while $V'_m = 1$ MV/m and $f_c = 0.8$. The main motivation for this case is to reduce the magnitude of the hysteresis loss. The total average pulsed power is about a factor of two less than the third case, however the weight of Metglas has increased slightly more than a factor of two.

The cases presented in Table 2 have been chosen to give some idea of the tradeoffs that are possible. Ultimately the choice of parameters will depend on minimizing the cost and meeting the requirements imposed by the rest of the μ^+–μ^- accelerator complex. The induction accelerator described in this paper has mostly been thought of as being applied to separate μ^+ and μ^- production channels, in which case two of them are required. However, provided the μ^+ and μ^- pulses are separated in time it is conceivable that a single accelerator structure driven by a bipolar pulsed power system could be used for μ^+ and μ^-. For this approach the pulsed power system would necessarily be replicated for each polarity so the cost savings would only be in the accelerator structure.

ACKNOWLEDGMENTS

REFERENCES

1. R.Palmer, D. Neuffer and J. Gallardo, *A Practical High-Energy High-Luminosity $\mu^+-\mu^-$ Collider*, Proc. of the Physics Potential and Development of a $\mu^+ -\mu^-$ Collider, (1995). W. Barletta is quoted in this paper as making the suggestion of using an induction linac rather than a low frequency rf linac for phase rotation.
2. J.G. Gallardo, private communication (1995).
3. Allied-Signal, Parsippany, New Jersey.
4. C.H. Smith, *Applications of Amorphous Magnetic Materials at Very-High Magnetization Rates*, Proc. of Magnetism and Magnetic Materials Conference, Boston (1989).
5. R.B. Miller, Intense Charged Particle Beams, Plenum, New York (1982).

LAWRENCE BERKELEY NATIONAL LABORATORY
UNIVERSITY OF CALIFORNIA
TECHNICAL & ELECTRONIC INFORMATION DEPARTMENT
BERKELEY, CALIFORNIA 94720